

Pore-scale modeling and upscaling of nonaqueous phase liquid mass transfer

Rudolf J. Held and Michael A. Celia

Environmental Engineering and Water Resources Program, Department of Civil and Environmental Engineering, Princeton University, Princeton, New Jersey

Abstract. A pore-scale model is developed to simulate mass transfer between two fluid phases in a porous medium. The approach uses a network description of the pore space and builds on explicit tracking of the fluid-fluid interfaces in the pore network. Mass transfer is computed as local mass fluxes across each interface, and transport equations are solved in the pore network by a characteristic method. The concept of stagnant-layer diffusion is used to describe the interface mass transfer, where calculated local concentrations control the rates of mass transfer. The model results predict dissolution fronts developed in column experiments of porous media initially at residual nonaqueous phase saturation. The definition of macroscopic mass transfer coefficients is investigated, and comparisons are made for rigorously upscaled quantities.

1. Introduction

Mass transfer from nonaqueous phase liquids (NAPLs) in contact with groundwater can produce a long-term source of groundwater contamination that is difficult to control or remediate. In these types of dissolution problems the mass transfer process is controlled by mass exchange kinetics at the level of discrete fluid-fluid interfaces, by the hydrodynamic flow regime of the aqueous phase, and by the amount and distribution of the nonaqueous phase in the pore space. Any model of this process should include each of these factors.

Existing methods for prediction of effective mass transfer coefficients rely on phenomenological source descriptions, with little account for the actual geometry of the fluids or the locations of fluid-fluid interfaces, or they rely on empirical equations obtained by fitting of dimensionless parameters to experimental data. Most continuum-scale predictive models employ lumped-parameter descriptions for the mass transfer between fluids, either from simplified mathematical solutions or experimental fits. *Miller et al.* [1990], *Powers et al.* [1991], and *Imhoff et al.* [1998] provided reviews of both theoretical and experimentally based expressions for macroscopic mass transfer coefficients. A few continuum models treat the mass transfer process as dissolution of discrete ganglia, where various shapes and sizes of nonaqueous phase ganglia are considered [e.g., *Powers et al.*, 1991; *Gvirtzman and Roberts*, 1991; *Geller and Hunt*, 1993]. Dissolution of NAPL droplets has also been simulated by lattice Boltzmann methods [cf. *Miller et al.*, 1998] within the resolution of single pore spaces.

A conceptual model for mass transfer from nonaqueous phase liquids at the pore scale was presented by *Feenstra and Guiguer* [1995] (see Figure 1). The nonaqueous phase, which is usually the nonwetting phase in natural porous media, will be trapped in pore spaces by capillary mechanisms. Dissolution of the NAPL occurs as groundwater flows past and through the zone of residual trapped NAPL. Mass transfer from NAPL in contact with the flowing water is conceptualized as predomi-

nantly dissolution rate-controlled. Mass transfer from NAPL in dead ends or stagnant regions of the groundwater flow will be diffusion-controlled and depend on the thickness of the layer of stagnant water [*Feenstra and Guiguer*, 1995].

This kind of conceptual model of pore-scale dissolution may be incorporated into the framework of pore-scale network models. Network models employ simplified representations of the pore space to model capillary displacement and flow dynamics. A typical transformation to a network geometry is illustrated in Figure 2, where the pore space is discretized into pore bodies and pore throats. To each pore body and throat a different size is assigned from representative pore size distributions. These pore elements are usually restricted to regular geometries for which analytical equations can be used for fluid volumes and interfacial shapes and areas. Within these pore-scale models all fluid-fluid interfaces are represented, and their movements are tracked explicitly in response to changes in fluid pressures [see, e.g., *Reeves and Celia*, 1996]. The present work extends the traditional network models to include mass transfer from the NAPL to the aqueous phase across fluid-fluid interfaces, miscible transport within the flowing aqueous phase, and systematic retraction of fluid-fluid interfaces as the volume of NAPL decreases because of the mass exchange.

A few numerical pore network models have been developed recently to study aspects of the dissolution problem. *Jia et al.* [1999a, 1999b] analyzed the mass transfer process over a range of flow conditions, i.e., varying Peclet numbers. They accounted for increased mixing and dissolution at fluid-fluid interfaces by adjusting local mass transfer rates, and they compared their results to experiments performed in two-dimensional etched-glass micromodels. Experimental results yielded locations of fluid-fluid interfaces. *Zhou et al.* [2000] developed a model that includes wedges and corners of wetting fluid, with concomitant mass transfer from and to these corner volumes. *Dillard and Blunt* [2000] used the conceptual model of *Zhou et al.* [2000] in a network model framework and studied dissolution over a range of flow conditions, demonstrating the importance of wedges of wetting fluid for cases of high Peclet numbers. *Dillard and Blunt* [2000] compared their results to column experiments performed by *Powers et al.* [1992, 1994] and demonstrated good agreement.

Copyright 2001 by the American Geophysical Union.

Paper number 2000WR900274.
0043-1397/01/2000WR900274\$09.00

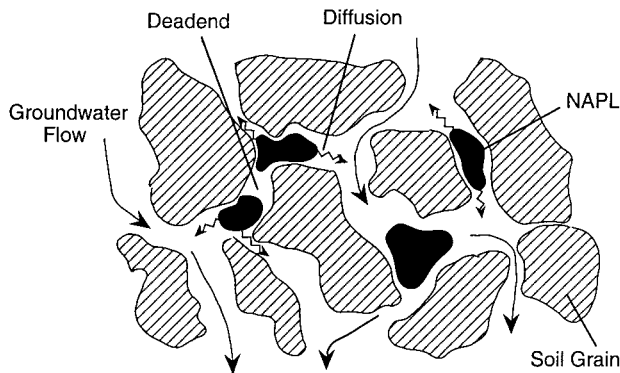


Figure 1. Conceptual model for dissolution at the pore scale (reprinted from *Kennedy and Lennox* [1997] with permission from Elsevier Science, based on the work of *Feenstra and Guiguer* [1995]).

In this paper, we present a computational pore-scale model for mass transfer that explicitly represents fluid-fluid interfaces, simulates solute transport in the aqueous phase within the pore space, and carefully accounts for the retraction of interfaces during the dissolution process. Our model is similar in general concept to the previous models referenced above, although it differs in that the interface retraction is applied systematically; based on physical rules for interface movement, the numerical algorithm for transport and the underlying pore geometries are different, and our application focuses on comparison to specific experiments, aspects of upscaling, and quantification of interfacial areas. Details of the model are presented in sections 2 and 3. We use the model to simulate a column experiment performed by *Imhoff* [1992], testing both the NAPL saturation predictions and the aqueous-phase solute concentrations. We also use the model to investigate different definitions of effective mass transfer coefficients at the continuum scale. In addition, we use the model to examine how NAPL-water interfacial area changes, as a function of saturation, during the dissolution process.

2. Theory

Given explicit fluid-fluid interface locations in a pore network, the mass transfer kinetics across these interfaces may be described with the theory of a stagnant boundary layer in the aqueous phase. In this type of description, NAPL interfaces are trapped by capillary forces at pore constrictions, and a stagnant aqueous phase is contained in the pore throat(s) next to the NAPL (see Figures 1 and 2). An aqueous-phase concentration equal to the NAPL component solubility limit, C_a^S ($M L^{-3}$), can be imposed as an interface boundary condition in the aqueous phase. This assumption implies a short timescale for thermodynamic equilibrium at the interface compared to the timescale for solute transport. The mass flux through the stagnant layer of aqueous phase may be expressed for a single-component NAPL as a first-order kinetic equation in the following form:

$$J_i = \frac{1}{A_{na,i}} \frac{dm_i}{dt} = k_{l,i} (C_a^S - C_{a,i}), \quad (1)$$

where for each interface i , J_i is the mass flux from the nonaqueous phase to the aqueous phase per unit interfacial area ($M T^{-1} L^{-2}$), $A_{na,i}$ is the interfacial area (L^2) between the

two fluid phases (nonaqueous and aqueous), m_i is the total mass of nonaqueous phase (M) dissolving into the aqueous phase, $k_{l,i}$ is a first-order mass transfer coefficient ($L T^{-1}$), and $C_{a,i}$ denotes the solute concentration ($M L^{-3}$) in the adjacent flowing aqueous phase, typically corresponding to the adjoining pore body. On the basis of the concept of an existing stagnant layer of aqueous fluid in the connecting pore throat with diffusion-controlled conditions, the local mass transfer coefficient $k_{l,i}$ in (1) is directly formulated from a one-dimensional form of Fick's law, with $k_{l,i} = D_m/l_i$. Here D_m is the molecular diffusion coefficient in the aqueous phase ($L^2 T^{-1}$), and l_i is the diffusion length of the stagnant aqueous phase (L). Note that a diffusion length in the network model is defined as the distance from the interface to the exit of the pore throat (see Figure 2), and thus it varies during the dissolution process. Interfacial areas, solute concentrations, and mass transfer rates are unambiguously defined at the pore level and can be used, via direct summation, to compute mass transfer over a simulated macroscopic sample. With respect to an elementary volume V (L^3) the mass transfer rate at the macroscopic scale can be derived from the pore-scale information as

$$\frac{1}{V} \sum_i [J_i A_{na,i}] = \frac{1}{V} \sum_i \left[A_{na,i} \frac{D_m}{l_i} (C_a^S - C_{a,i}) \right], \quad (2)$$

with only D_m and C_a^S taken as constants.

The formulation of an effective mass transfer rate coefficient at the macroscopic scale commonly decouples local concentration gradients from the mass transfer formulation across interfaces, i.e.,

$$\frac{1}{V} \sum_i [J_i A_{na,i}] \equiv K_{\text{eff}} (C_a^S - \langle C_a \rangle), \quad (3)$$

where angular brackets denote an average quantity measured over the macroscopic volume (i.e., over a representative elementary volume). The measurement techniques in the field or the laboratory normally correspond to such averages, taken over the volume of many pores. Laboratory investigations, which obtain K_{eff} (T^{-1}) from measured data, have only mac-

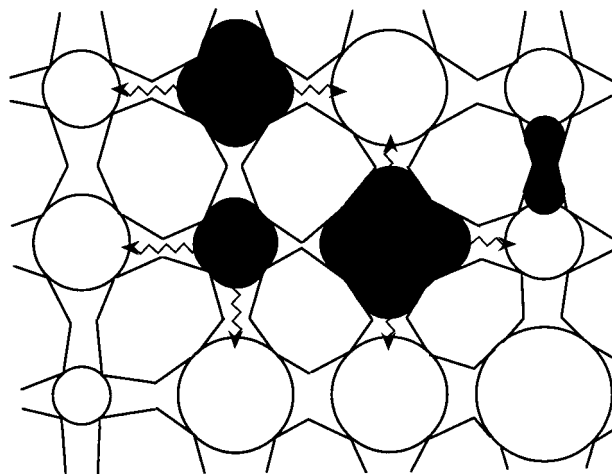


Figure 2. Schematic of a lattice network section, representing the conceptualization of Figure 1. Solid areas represent nonaqueous phase.

rosopic information available, corresponding to the summation on the left-hand side of (3). A very attractive aspect of pore-scale network models is that the local information is provided explicitly, and K_{eff} can be solved for by rearrangement of (2) and (3) as

$$K_{\text{eff}} = \frac{\frac{1}{V} \sum_i \left[A_{na,i} \frac{D_m}{l_i} (C_a^S - C_{a,i}) \right]}{(C_a^S - \langle C_a \rangle)}. \quad (4)$$

The coupling between local concentrations and interface mass transfer is therefore preserved in the upscaling to macroscopic mass transfer coefficients.

In lumped-parameter approaches [see *Miller et al.*, 1990; *Powers et al.*, 1991] a standard macroscopic mass transfer rate coefficient, denoted by K_l (T^{-1}), is defined as a function of interfacial area and average mass transfer coefficients, independent of concentration gradients:

$$K_l = a_{na} \langle k_l \rangle, \quad (5)$$

where a_{na} ($L^2 L^{-3}$) represents the specific interfacial area (area per total elementary volume V) and $\langle k_l \rangle$ is the average mass transfer coefficient of the sample ($L T^{-1}$). The lumped description as K_l typically circumvents the problem of requiring knowledge about a_{na} by adopting a phenomenological formulation of the mass transfer, wherein interfacial area is replaced by a function involving phase saturation in the general form:

$$K_l = \beta_1 \theta_n^{\beta_2}, \quad (6)$$

where θ_n ($L^3 L^{-3}$) is the nonaqueous phase volume fraction. The coefficient β_1 (T^{-1}) becomes a function of system properties, like porous medium parameters, molecular diffusion, and aqueous phase velocity (i.e., including Reynolds number), and the exponent β_2 (dimensionless) is assumed to be a function of porous medium properties. A brief review on lumped-parameter descriptions is given by *Inhoff et al.* [1998]. An equivalence of the rate coefficients K_{eff} and K_l , with the former measured from experiments and the latter hypothesized in relation to system parameters, is frequently presumed in the investigations of dissolution problems.

With the detailed pore-scale information present in (2), we may calculate a mass transfer rate coefficient analogous to K_l in (5), such that

$$K_l = \frac{\sum_i A_{na,i} \left\langle \frac{D_m}{l} \right\rangle}{V}, \quad (7)$$

where $\langle k_l \rangle$ has been replaced by $\langle D_m/l \rangle$ from the concept of a stagnant-layer diffusion region. This description of macroscopic mass transfer can be quantitatively compared with the above, rigorously defined, effective mass transfer rate coefficient K_{eff} . A comparison is given in section 4.2.

3. Methods

The pore-scale network model for dissolution has three major components: the capillary displacement model that provides fluid distributions and hydrodynamic flow conditions, the mass transfer model that describes mass transfer across individual fluid-fluid interfaces and associated interface retraction, and the solute transport model for the flowing aqueous phase

in the pore network. In sections 3.1–3.3 we describe each of these three model components.

3.1. Capillary Displacement

The present model builds on the previously documented pore-scale model for immiscible displacement used by *Reeves and Celia* [1996] and *Reeves* [1997], with a network discretization of the pore space as a cubic lattice with spherical pore bodies and connecting biconical pore throats (see Figure 2 for a section through the three-dimensional pore space). The distribution of pore sizes includes pore body–pore throat correlations. The distribution of pore body radii is generated according to a beta distribution with upper and lower size limits, and pore throat radii are correlated in size to the connecting pore bodies as described by *Reeves* [1997]. This procedure generates a fairly homogeneous pore structure that we used herein as a representation of a well-graded, uniformly packed porous medium column, corresponding to the experimental porous medium to which we compare our numerical results.

Fluid occupancies in the pore network are determined by quasi-static displacement rules. For an imposed difference in fluid reservoir pressures, fluid interfaces are adjusted until equilibrium positions are established throughout the network. Saturations and interfacial areas are then calculated for the given reservoir capillary pressure. Given an equilibrium distribution of the fluids and fluid interfaces, a flow field can be simulated by application of an external pressure gradient in a connected phase. This pressure gradient is presumed to be sufficiently small to have insignificant influence on interface locations. Poiseuille flow is assumed in all pore throats, and mass conservation equations are written for each pore body in the network. This leads to a system of equations for the pressures at pore bodies, which can be solved by standard matrix methods. The associated flow velocities in the pore throats are then determined from the nodal pressures in the pore network. Such a procedure provides both the detailed flow field and an estimate of relative permeability. For a comprehensive description of the displacement model, including calculation of relative permeabilities and interfacial areas, see *Reeves* [1997].

The model may be used for arbitrary drainage or imbibition cycles. For the current work, a primary drainage sequence is followed by main imbibition to generate a distribution of residual nonaqueous phase, which is characteristic for the particular pore structure of the porous medium.

3.2. Dynamic Ganglia Dissolution

The displacement model gives explicit positions and configurations for all fluid-fluid interfaces in the network. Mass transfer is allowed to occur across every one of these interfaces, depending on the local conditions. Because dissolution from a state of residual NAPL saturation has been treated extensively in experimental work, we focus on this situation, but we are not limited to it in the simulation of mass transfer processes.

Whenever a ganglion of NAPL is formed in the displacement model by isolation from its fluid reservoir, the capillary pressure value at the time of isolation is assigned to that ganglion. In the absence of mass transfer, that assigned capillary pressure is considered to be independent of any subsequent changes to reservoir pressures. However, during dissolution the capillary pressure associated with a trapped ganglion is modified as a function of the volume of NAPL dissolved and the local pore geometry. The dissolved volume is computed

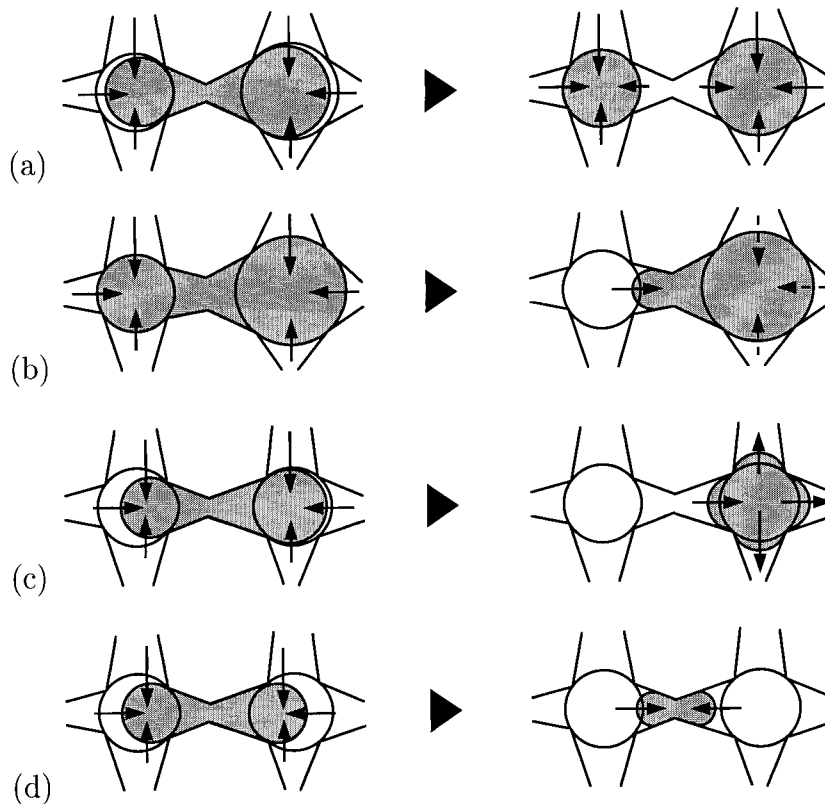


Figure 3. Schematic of rules during ganglia dissolution: (a) Snap-off of nonwetting phase in pore throats. (b) Volume retraction to large pore bodies. (c) Shift of volume past pore throat constrictions. (d) Trapping of nonwetting phase in pore throats. Shaded areas represent NAPL.

according to (1), with $C_{a,i}$ being the aqueous concentration in the pore body adjacent to the interface and l_i and $A_{na,i}$ being the one-dimensional diffusion length and fluid-fluid interfacial area, respectively, for an individual interface i . The diffusion length associated with every interface is calculated from the interface location and the average distance in the pore throat to the flowing aqueous phase at the entrance of the adjacent pore body. This assumes stagnant aqueous phase in a pore throat associated with an interface. The effective diffusion length and corresponding interfacial area for mass transfer are updated based on the retraction dynamics of the interface, while the local concentrations are computed by the miscible transport algorithm as described in section 3.3.

When a ganglion shrinks in size during dissolution, the interfaces of that ganglion have to adjust. This is accompanied by changes in interfacial area and curvature and hence in ganglion capillary pressure. For interfaces located in the biconical pore throats, we can apply the Young Laplace equation to relate a capillary pressure to interface positions. For more complex interfacial geometries within pore bodies we have derived lower and upper bounds for interfacial areas and capillary pressure, respectively; see *Held and Celia* [2001] for details. Recall that the value of capillary pressure for each isolated ganglion is uncoupled from the NAPL reservoir pressure. Therefore the external reservoir pressures no longer control the capillary pressure of the residual NAPL and should not be used in the description of macroscopic capillary pressure. Since the capillary pressures are known locally, an associated capil-

lary pressure for ganglia, or the entire sample, can be calculated [see *Hassanizadeh and Gray*, 1993; *Held and Celia*, 2001].

To provide a physical framework for the retraction of interfaces as NAPL ganglia dissolve, minimum energy principles, or energy dissipation, associated with the interface configuration can be applied [*Mohanty et al.*, 1987; *Li and Wardlaw*, 1986a, 1986b]. In updating interface locations because of shrinkage of a ganglion we include the mechanisms of snap-off of the nonaqueous phase in pore throats, preferential volume retraction into large ganglion sites, shift of nonaqueous phase volumes to stable interface positions, and trapping of the nonaqueous phase in pore throats. These dynamic mechanisms are related to the local pore structure by the following criteria: (1) If a fluid-fluid interface resides in a pore body and the NAPL is connected through a pore throat to other NAPL-filled pore bodies, the snap-off criterion is given by

$$\frac{P_t}{P_b} \equiv \frac{r_b}{r_t} > 2.0, \quad (8)$$

where P is the capillary pressure (FL^{-2}) for piston displacement in either the pore body P_b or the pore throat P_t , expressed equivalently using the pore body and pore throat radii (L), r_b and r_t , respectively [cf. *Lenormand et al.*, 1983; *Mohanty et al.*, 1987]. The critical ratio of 2.0 was found by *Mohanty* [1981] for oil-water systems and is used herein for our computations. For larger connected ganglia this criterion can lead to formation of separated singlets in the process of NAPL dissolution (see Figure 3a). (2) If the connecting pore throat

radius is larger than required for a snap-off condition in the first criterion, a criterion for continuous volume retraction to an adjacent pore body is tested. We compare the sizes of the connected pore bodies and throats, given the pore body and pore throat radii and geometry, to test whether the volume residing in the smaller pore body plus the volume of the pore throat could be accommodated in the larger pore:

$$V_{b,i}(r_i) > V_{b,j}(r_j) + V_{t,ij}(r_{ij}, r_i, r_j), \quad (9)$$

where V_b and V_t represent volumes (L^3) of pore bodies and throats, respectively, r denotes the radius, and i and j denote adjacent pore bodies. In this criterion the interfaces with large curvature in the smaller pore are less favored than interfaces associated with the larger neighboring site. The NAPL volume retracts continuously to the larger pore space (see Figure 3b). (3) When an interface can recede through a pore throat and it reaches the constriction in the pore throat, the high interfacial curvature may not be stable inside the divergent portion of the pore throat; in this case the volume in the pore throat is shifted to the connected pore body. This criterion results in a jump in interface locations, and in interfacial areas and capillary pressure, for the ganglion (see Figure 3c). (4) If two connected pore bodies occupied by NAPL dissolve simultaneously, interfaces are allowed to reside in both of the diverging portions of the pore throat, balancing the forces acting at the two interfaces. The NAPL is presumed trapped in the pore throat location, until fully dissolved (see Figure 3d).

The above criteria provide a consistent decision framework for the dissolution process in the pore-scale network model. For example, they determine whether a ganglion breaks up into multiple ganglia or simply shrinks as a single entity. These phenomena can affect the dissolution sequence and also the overall dissolution time. The diffusion lengths and corresponding interfacial areas vary in the pore space, as the volume of nonaqueous-phase ganglia changes. Mass transfer limitations, in turn, become more important with increasing time, as diffusion lengths may increase and interfacial areas become smaller.

The mobilization of shrinking NAPL droplets during the process of dissolution is not considered in the model in its present formulation. This is supported by experimental observations. Mobilization of dissolving NAPL ganglia was not observed by *Imhoff* [1992] for flow rates typical in natural aquifers. Similarly, *Kennedy and Lennox* [1997] conducted visualization experiments on dissolving NAPL droplets at Darcy velocities between 0.29 m d^{-1} and 720 m d^{-1} and found no evident mobilization in most experiments. *Jia et al.* [1999a] saw mobilization of some ganglia at high capillary number conditions in micromodel studies; the two-dimensional, etched-glass model with straight pore throat geometries can partly account for this effect. At present, we restrict our model to low flow rates and relatively high interfacial tensions and do not account for mobilization of droplets.

3.3. Solute Concentration Field

The dissolved NAPL concentration in the aqueous phase at each pore is computed with a type of characteristic tracking algorithm in combination with a path line method [*Delay et al.*, 1994; *Johnson et al.*, 1994]. Over a time Δt , dissolved nonaqueous phase mass from each interface diffuses into the aqueous-phase flow field, serving as the source of NAPL in the aqueous phase. We assign zero aqueous-phase velocity to the stagnant

regions and formulate advection in the flowing domain of the pore network in terms of residence times. The pores are modeled as completely mixed, and the probability, or mass fraction, to reach an adjacent pore is taken to be proportional to the fraction of the total aqueous-phase flux in that direction. All possible paths along streamlines over a time step Δt are independently recorded. This algorithm is fully volume and mass conservative, and the characteristic formulation enables the use of large time steps. At small time steps the solution converges to a standard finite difference formulation.

In the solute transport model we use lattice, or pore, elements, i.e., a pore body plus half the connected biconical throats, to discretize the pore space of the flowing aqueous phase. Advective solute transport equations, which apply to each element, can be written as

$$V_{a,i} \frac{\Delta C_{a,i}}{\Delta t} + \sum_{j \in N_i} [Q_{ij} C_{a,j}] = \sum_{j \in M_i} [J_j A_{na,j}]. \quad (10)$$

On the left-hand side of (10), $V_{a,i}$ denotes the volume (L^3) of the lattice element i containing the aqueous phase (excluding stagnant regions associated with interfaces and nonaqueous-phase volumes); N_i is the number of throats connected to site i ; Q_{ij} refers to the volumetric aqueous flow rate ($L^3 T^{-1}$) in the throat between sites i and j ; M_i is the number of interfaces connected to site i ; and $C_{a,i}$ and $C_{a,j}$ refer to aqueous concentrations in appropriate pore elements. The flow rate Q_{ij} is analytically computed from the pressure drop between i and j and the fluid conductance G_{ij} for the throat ($L^5 F^{-1} T^{-1}$), such that $Q_{ij} = G_{ij} \Delta P_{ij}$. The fluids are assumed incompressible; hence the mass balance at each pore element may be expressed as a volumetric balance:

$$\sum_j Q_{ij} = 0, \quad j = 1, 2, \dots, N_i. \quad (11)$$

This matrix equation is solved for appropriate pressures at the pore sites under imposed pressure or flux boundary conditions. It provides the distributed flow field for the particular pore structure and wetting fluid distribution in the pore network.

To compute aqueous-phase concentrations, the pore volume occupied by the aqueous phase is discretized in lattice or pore elements, as described above. For each of these elements, with associated volume $V_{a,i}$, an overall residence time of the individual flow paths through the element is calculated as t_i , based on the computed flow field. Here $t_i = V_{a,i}/Q_i$, with $Q_i = \sum_j (Q_{ij})_{\text{in}} = \sum_j (Q_{ij})_{\text{out}}$ being the overall flow rate through that lattice element. The advective transport algorithm is formulated as a characteristic method, which follows the position of a fluid volume in the network after a time step Δt . The solute mass of an element, $m_o = C_{a,o} V_{a,o}$, at time t is then allocated to the location of that volume at time $t + \Delta t$:

$$m_i = 0, \quad t^+ \in [t, (t + \Delta t)],$$

$$m_i = m_o \frac{Q'_i t_i}{Q_o t_o}, \quad t^+ \in [(t + \Delta t), (t + \Delta t) + t_o], \quad (12)$$

where m_i is the addition of mass to any element i , $t^+ = t + \sum_j t_j$ is the elapsed time given by the summation of residence times along the individual paths traversed by the mass in the originating element, Q'_i/Q_o represents the fraction of the volumetric flow in a splitting path reaching element i , and subscript o indicates the solute mass, flow rate, and residence time of the originating element. Equation (12) is applied for all possible

originating elements, thereby redistributing all mass from its locations at time t to new locations at $t + \Delta t$.

The source term on the right side of (10) exists only for elements that have fluid-fluid interfaces located adjacent to them. There the source term is given by a discrete form of (1):

$$J_j A_{na,j} = \frac{\Delta m_j}{\Delta t}, \quad j = 0, \dots, M_i, \quad (13)$$

where M_i is the number of interfaces associated with the pore element i , and Δm_j is the mass added to the element from an adjacent interface, over time Δt . With appropriate assumptions about the local concentration field, (1) may be solved to obtain Δm_j , the transient addition of mass to the volume V_i after time Δt . Dissolved mass from the source is then partitioned to elements along a flow path based on residence time in the elements for the time Δt , so that the mass retained at each element i is

$$m_i = \Delta m_o \frac{Q'_i}{Q_o} \frac{t_i}{\Delta t + t_o}, \quad (14)$$

where subscript o indicates the input of dissolved mass, flow rate, and residence time at the source input element and Q'_i/Q_o represents the fraction of the volumetric flow reaching element i from the originating element (o). The mass input from fluid-fluid interfaces results in a uniform concentration along the pathlines in the pore network, $C'_i = m_i/(Q'_i t_i)$. This is consistent with a continuous source over the time step Δt .

With the mass already in solution (equation (12)) and the new mass added via dissolution (equation (14)) accounted for, the aqueous phase concentration in every pore element i at $t + \Delta t$ may be obtained by superposition of (12) and (14):

$$C_{a,i} = \sum \frac{m_i}{V_{a,i}}. \quad (15)$$

Application of this algorithm for the entire network provides the concentration field in the aqueous phase. The structuring of the above algorithm in separate computations of advective mass transport and continuous source input facilitates variable weighting between an implicit and explicit formulation of the source functions in time; that is, the aqueous-phase concentration $C_{a,i}$, used in the solution of (1), is implemented as

$$C_{a,i} = \xi(C_{a,i})^{t+\Delta t} + (1 - \xi)(C_{a,i})^t, \quad (16)$$

with $\xi = 0$, explicit, and $\xi = 1$, implicit. For the application in this work we used the explicit source input formulation ($\xi = 0$).

In this approach, no matrix equations need to be assembled or solved for nodal concentrations because all calculations are based on individual flow paths and residence times. While pore-scale diffusion is not modeled, hydrodynamic dispersion and associated mixing arise naturally from the tortuosity and variable velocity in the pore network. Matrix equations for the pressure field in the network are updated and solved whenever NAPL is fully dissolved from any pore element.

4. Results

We have applied this model to simulate the dissolution experiments reported by *Imhoff* [1992] and *Imhoff et al.* [1994]. This comparison involves a single-component NAPL, whereas the previous descriptions would apply equally to individual

Table 1. Parameters of Experiment 1 of *Imhoff* [1992] Used in the Numerical Model

Parameter	Description	Value
D_m^m	molecular diffusivity in H ₂ O	$0.935 \times 10^{-9} \text{ m}^2 \text{ s}^{-1}$
C_a^m	TCE solubility in H ₂ O	1.277 kg m^{-3}
ρ_n	TCE density	1465 kg m^{-3}
μ_n	TCE viscosity	$0.58 \times 10^{-3} \text{ kg m}^{-1} \text{ s}^{-1}$
σ_{na}	surface tension	$35.0 \times 10^{-3} \text{ kg s}^{-2}$
q_a	Darcy flux	0.52 m d^{-1}
L	column length	0.03 m
ϕ	column porosity ^a	0.346 ± 0.004
S_n	residual TCE saturation ^a	0.141 ± 0.014

^aSample porosity ϕ and residual TCE saturation S_n in the model result from the displacement simulation in the pore structure (see Table 2).

species in a multicomponent NAPL. In addition to comparison of saturation profiles and aqueous concentrations, we have computed values for the different definitions of macroscopic mass transfer rate coefficients, and we have estimated interfacial areas directly as the dissolution proceeds. Results from these calculations are presented and discussed in the remaining sections of the paper.

4.1. Comparison to Experiments

To demonstrate the overall behavior of the network model for dissolution, a laboratory experiment of *Imhoff* [1992] has been simulated with the numerical pore-scale model. The experiment involved a fine-grained Ottawa sand, which was initially saturated with water. The sample was drained, with trichloroethylene (TCE) displacing water upward. Water was then reintroduced from the top, and the main imbibition curve was followed until residual saturation of TCE was achieved. Solute concentrations of the NAPL in the aqueous phase were allowed to equilibrate under no-flow conditions. Continuous flushing with clean water was then initiated to produce the dissolution of TCE. Changes in fluid saturations along the column were measured with a dual-gamma attenuation system. The experimental system parameters are summarized in Table 1.

To model this system, a three-dimensional network model with $90 \times 40 \times 40$ pore bodies was constructed, corresponding in physical dimensions to the experimental column length of 3 cm and a model cross section of approximately $1.2 \text{ cm} \times 1.2 \text{ cm}$. Length scales in the pore size distributions are taken from the reported grain-size distribution of the porous medium and length ratios conforming to a random packing of nearly uniform sphere sizes (see Table 2 for model parameters). To test

Table 2. Model Parameters for Pore Space Representation^a

Parameter	Description	Value
B	beta distribution of pore body radii	
	mean	0.094 mm
	standard deviation	0.014 mm
	minimum	0.05 mm
	maximum	0.12 mm
d	lattice spacing	0.3 mm
ϕ	sample porosity	0.315 ± 0.004

^aResidual TCE saturation in the sample $S_n = 0.143 \pm 0.011$ after primary drainage and main imbibition displacement sequence.

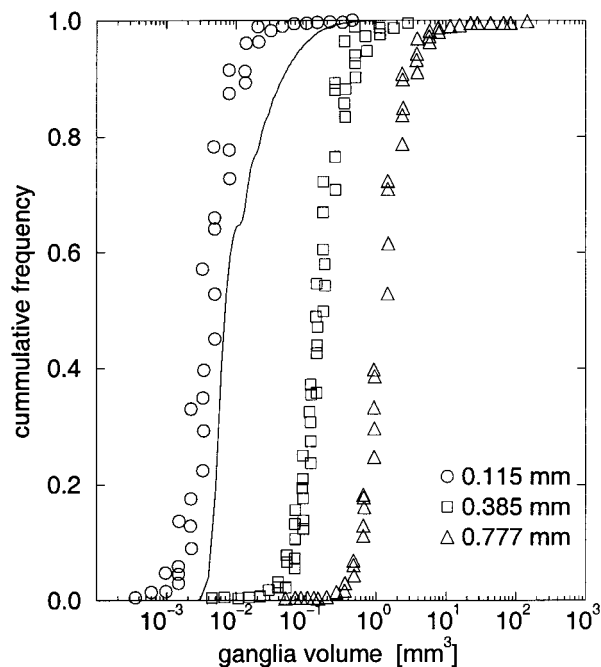


Figure 4. Ganglia volume distribution for glass beads of various diameters (symbols) (reprinted from *Mayer and Miller* [1992] with permission from Elsevier Science). The solid line represents the ganglia distribution from our network model, based on a porous medium with grain-size diameters between 0.30 mm and 0.42 mm (mesh size 50–40).

the network model for its ability to produce a realistic residual distribution of the NAPL, we compared the generated distribution of trapped ganglia with data of *Mayer and Miller* [1992] (Figure 4). The simulated ganglia distribution is within the range of corresponding data for styrene ganglia in fine-grained granular material. The experiments of *Imhoff* [1992] did not provide a measurement of ganglia-size distributions. However, as seen in Figures 6 and 7 below, the average residual NAPL saturation of approximately 0.14 is captured well by the model.

In the dissolution simulation a hydraulic pressure gradient in the aqueous phase was imposed across the network to match the measured Darcy flux imposed in the laboratory experiments. The flux field in the model was continuously recalculated as NAPL-filled pores became open to aqueous flow after dissolution. Thus the local flux distribution within the network changes as the dissolution proceeds, although the overall flux through the network was held at the experimental value of 0.52 m d^{-1} (for experiment 1 of *Imhoff* [1992]). As initial conditions, the aqueous concentration was set to the solubility limit everywhere in the sample. Clean water enters the top boundary, and a dissolution front develops and moves through the sample as concentration gradients in the aqueous phase evolve. Figure 5 gives the measured effluent concentrations at the outlet (after a mixing volume) for experiment 1 [*Imhoff*, 1992] along with the simulated concentration profiles for a series of horizontal slices in the network model. The computed concentration profiles are presented for each millimeter of the top 27 mm of the model, with concentrations averaged over the entire horizontal area. These profiles show a smooth and consistent behavior, corresponding to development of a dissolution front. The simulated concentrations at the outlet closely match the measured concentrations.

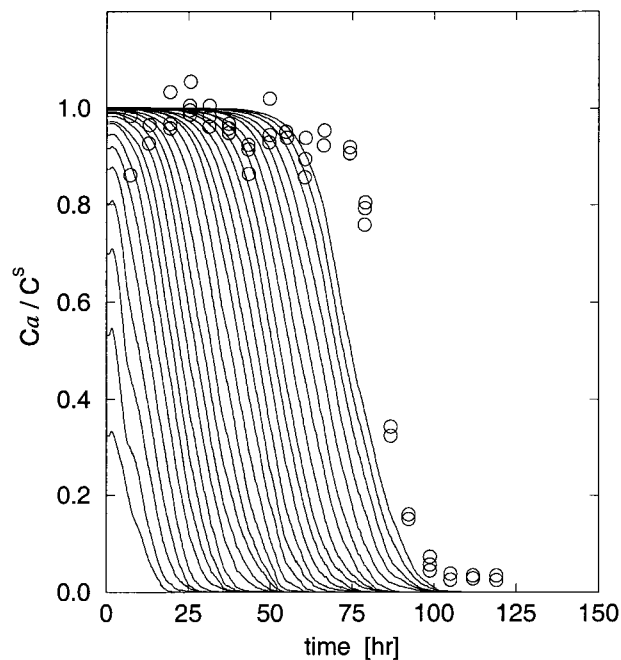


Figure 5. Concentration profiles of trichloroethylene (TCE) in the aqueous phase predicted by the network model. Lines correspond to horizontal averages over 1 mm slices, taken at 1 mm increments along the column length. Symbols give measured effluent concentrations at the outlet (from experiment 1 of *Imhoff* [1992]) (taken from *Imhoff* [1992]).

Figure 6 provides measured saturation profiles from the same experiment of *Imhoff* [1992], determined from gamma-ray attenuation over horizontal slices of the column 1 mm in thickness. For comparison, Figure 7 shows the results from the network model simulation of the dissolution experiment. Saturations are computed as moving averages along the sample, with the averages taken over approximately 1 mm slices to correspond to the experimental measurements. The fluctuations seen in initial residual saturations are in agreement with observations of residual NAPL distributions with respect to the averaging volume [*Mayer and Miller*, 1992]. The development and propagation of a dissolution front with time, or, equivalently, with the number of pore volumes flushed, is clear in Figures 6 and 7, with the network model capturing the front and its propagation speed well. Both the experimental system and the network model required slightly more than 210 pore volumes to dissolve the residual NAPL. Overall, the results are excellent, with a very close match between experimental and model profiles over the entire duration of the experiment.

The results presented here are from a single realization of the pore structure. It is noteworthy that we only fitted the pore-space morphology in this approach, then used physical descriptions consistent with the scale of representation without any calibration. Our choice of pore space parameters was based on extraction of pore networks from sphere packs [see *Reeves*, 1997]. We noted that residual NAPL saturation is sensitive to pore structure and to fluid properties, such as interfacial tension and contact angle.

4.2. Upscaling of Mass Transfer

Knowledge of actual fluid-fluid interfacial areas and interface locations, necessary for determination of K_f in (5) and (7),

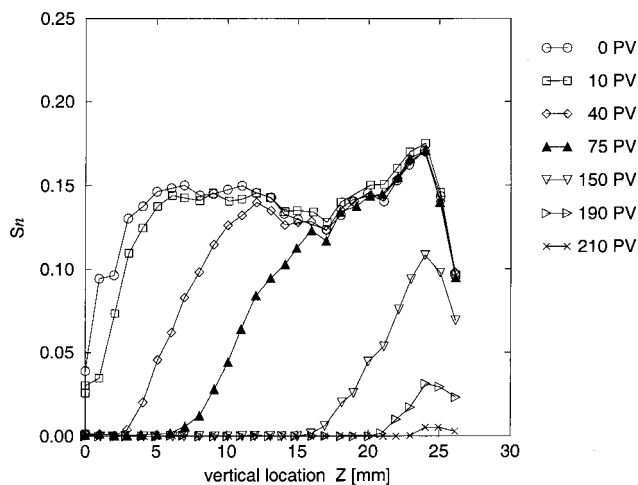


Figure 6. Saturation profiles of TCE versus depth, at different times, for experiment 1 of *Imhoff* [1992]. Time is given in number of pore volumes, PV (taken from *Imhoff* [1992]).

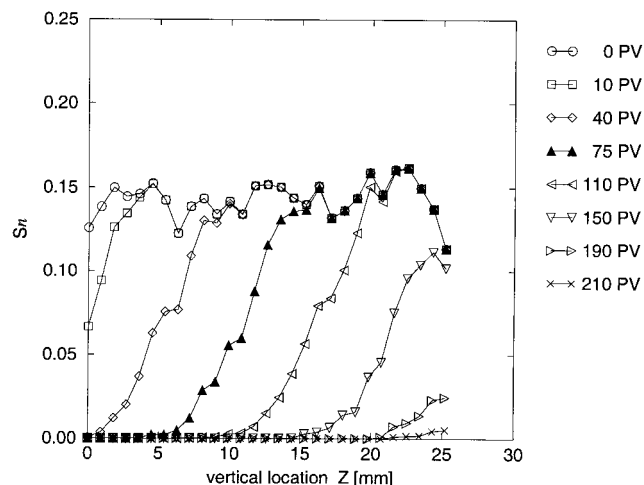


Figure 7. Saturation profiles of TCE versus depth, for different times, predicted by the network model. Time is given in number of pore volumes, PV.

is typically not measurable and therefore not known for porous media systems. However, the network model allows such information to be computed directly. Figure 8 presents total water-NAPL interfacial area and average diffusion lengths, as a function of volumetric NAPL content, θ_n . The total interfacial area shown in Figure 8 is related to the dissolution sequence. These data were calculated throughout the dissolution process and are given per unit volume of the entire sample; other averages, for example, over the 1 mm measuring thickness of *Imhoff* [1992], can also be computed as needed. The data indicate a near-linear relationship between interfacial area and saturation over the considered range of θ_n . Because the interfacial information is provided explicitly, the mass transfer rate coefficient K_l can be computed directly, as can the coefficient K_{eff} . In this section, we use the network model to calculate both of these coefficients, compare the two definitions, and investigate the behavior of these macroscale coefficients as a function of averaging volume.

Figure 9 presents both K_l and K_{eff} , determined over the volume of the entire network. The coefficient K_l is decoupled from the local concentration gradients (see (5) and (7)), while K_{eff} is computed from (4) and therefore preserves the coupling to the local concentration field. Computed values of these two coefficients show a different magnitude and different functional dependency on NAPL content. In order to examine each of these coefficients more closely, we may compare them to the data of *Imhoff* [1992], also reported by *Imhoff et al.* [1994]. Because the experiments of *Imhoff* [1992] or *Imhoff et al.* [1994] did not include any measures of interfacial area, the coefficients that were derived from those experiments are equivalent to K_{eff} . *Imhoff* reported estimates of K_{eff} for each of the 1 mm slices used for measurements; these data are plotted in Figure 10. While these data show significant scatter, the lower values are generally more reliable. To compare these data to the coefficients computed with the network model, we calculated the mass transfer rate coefficients for each 1 mm slice of the network model. The results for K_{eff} are shown in Figure 11. The model-predicted values of K_{eff} fall within the spread of the experimental values found by *Imhoff* [1992], and the general behavior of the coefficients as a function of position along the column is comparable. Results for K_l , shown in

Figure 12, display a similar behavior, although the values of K_l are consistently larger than the corresponding K_{eff} values.

It is notable that the values of K_{eff} reported in Figure 9, which were based on an averaging volume corresponding to the entire sample, are lower than those reported in Figure 11, which are based on slice averages at different vertical locations. Slice averages describe the mass transfer as the dissolution front passes and are thus capturing local (macroscopic) dynamics associated with the frontal movement. Averaging over regions outside the active mass transfer zone leads to reduction of the overall mass transfer rate. This suggests a restricted scale where a macroscopic mass transfer coefficient is representative and calls into question the validity of this macroscopic coefficient for arbitrary upscaled volumes. Recent work

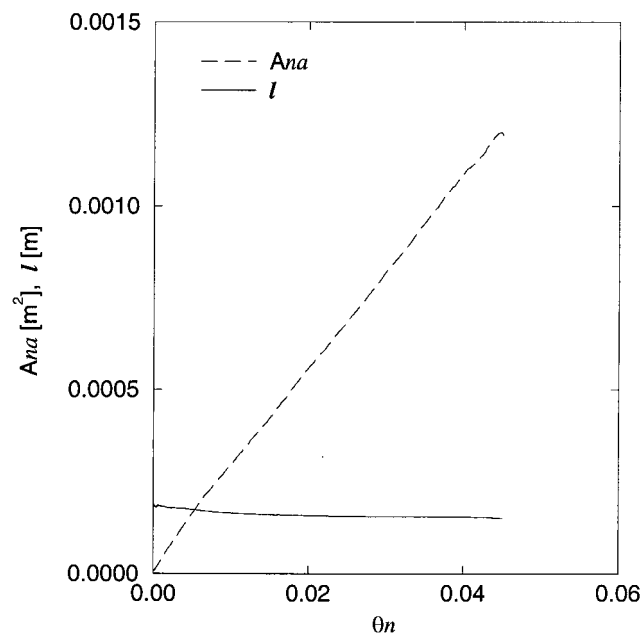


Figure 8. Network model prediction of average diffusion length, l , and total interfacial areas, A_{na} , in the dissolution process.

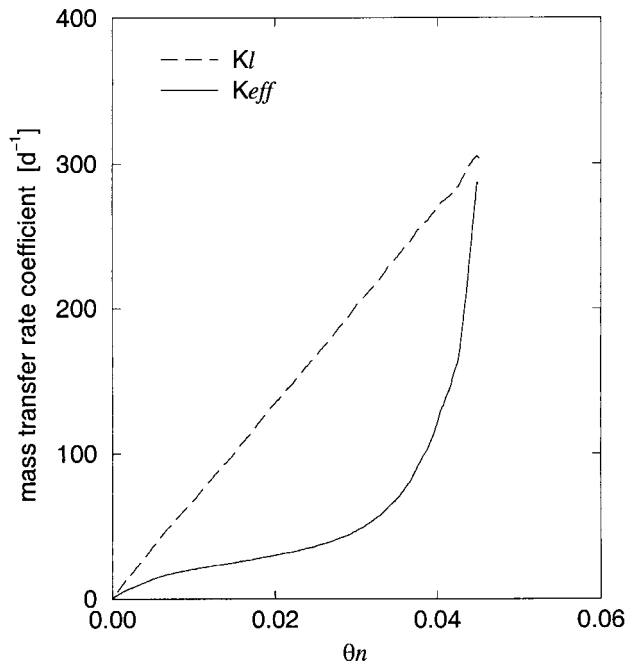


Figure 9. Network model prediction of macroscopic mass transfer rate coefficients, K_l and K_{eff} , with respect to total sample volume.

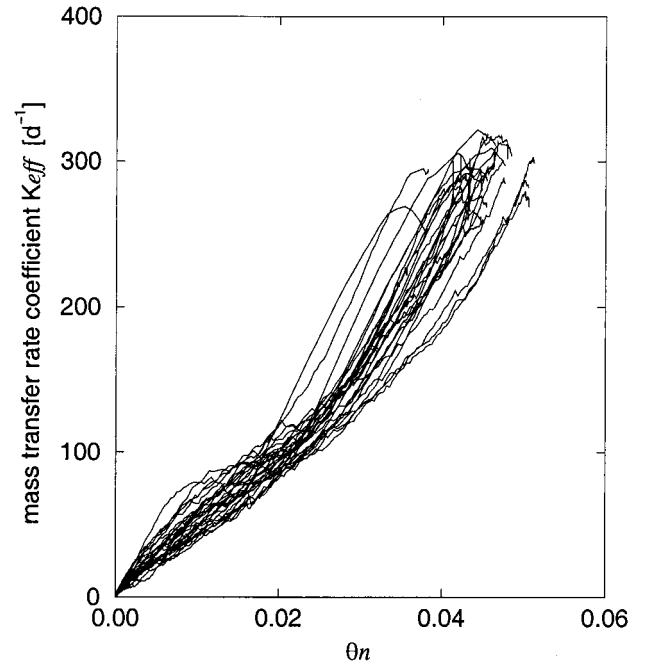


Figure 11. Network model prediction of the macroscopic mass transfer rate coefficients, K_{eff} , with respect to vertical sample location.

of, for example, *Young and Ball [1995]* or *Soerens et al. [1998]* has raised similar questions by showing dependence of the macroscopic mass transfer coefficient on aqueous phase velocity and on distance into the mass transfer zone. In the network model simulation we see the propagation of a mass transfer front, where cross-sectional (slice) averaging provides an appropriate description, such that stable areal averages are ob-

tained for K_{eff} (Figure 11). However, volume averages fail to respect local frontal behavior, and may only be expected to apply when many local fronts are statistically captured and therefore become independent of the shape of the macroscopic averaging volume, and time. This type of scale dependence is not seen in the results for K_l ; the sample-averaged values in Figure 9 compare well with the slice averages shown

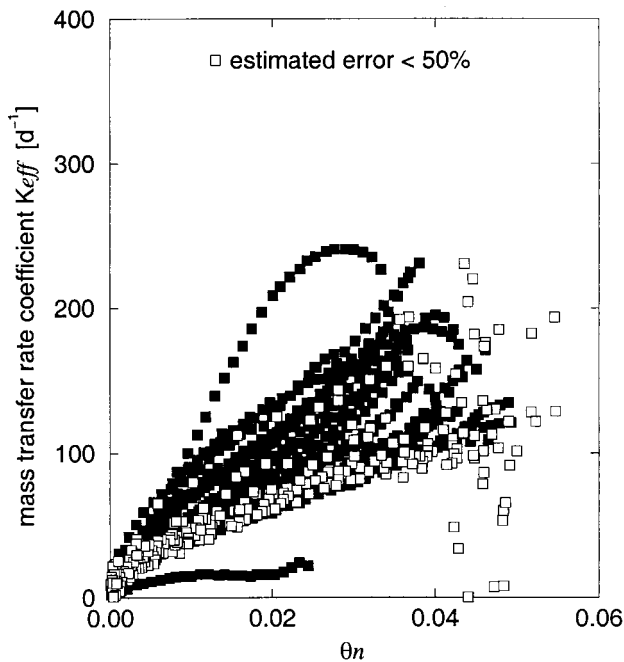


Figure 10. Macroscopic mass transfer rate coefficients, K_{eff} , with respect to vertical column locations for experiment 1 of *Imhoff [1992]* (taken from *Imhoff [1992]*).

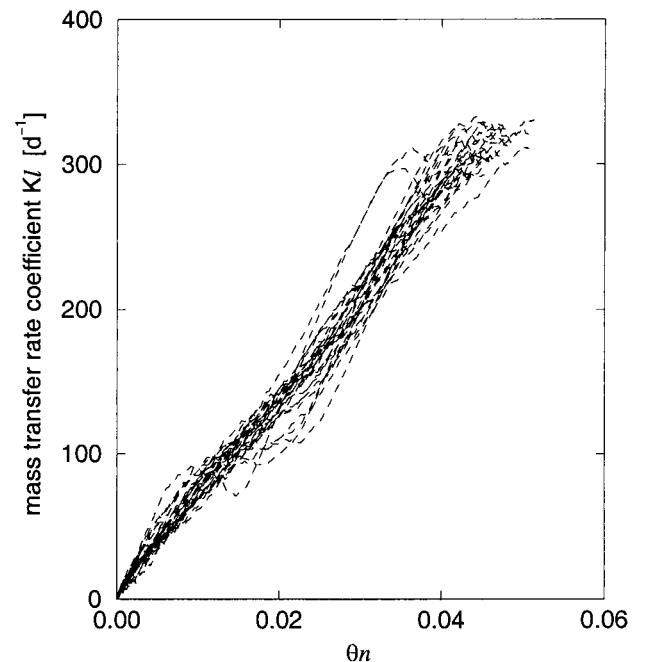


Figure 12. Network model prediction of the macroscopic mass transfer rate coefficients, K_l , with respect to vertical sample location.

in Figure 12. This appears to be consistent with a standard conditional convergence for averaged system properties ($\langle k_l \rangle$ in (5)).

5. Discussion and Conclusions

Pore-scale network models offer opportunities to study transport phenomena in novel ways, because detailed information is available at the pore scale. As such, consistent upscaling can be performed, based on physical processes that are defined at the appropriate scales. In this work, we have used a pore-scale network model to simulate fluid-fluid displacements through both drainage and imbibition cycles, producing a residual NAPL saturation in a sample porous medium. We then used mass transfer descriptions appropriate for individual fluid-fluid interfaces to model mass transfer from the NAPL to the aqueous phase and subsequent miscible transport in the flowing aqueous phase. This allowed for comparison of model results with previously reported experiments involving dissolution, as well as additional investigations involving quantities that are difficult or impossible to measure, including fluid-fluid interfacial areas, local mass transfer coefficients, and local concentration gradients. We also used the model to investigate upscaling of the mass transfer coefficients.

Comparison of our model results with laboratory experiments of NAPL dissolution showed excellent agreement with respect to development and propagation of the dissolution front, including both saturation profiles and aqueous concentrations. The effective mass transfer coefficients derived from the model also fell within the range of values measured in the experiments. In our model the pore structure statistics were chosen to correspond to a homogeneous, fine-grained porous medium. Agreement with the measured NAPL saturation at residual, and the reasonable distribution of ganglia sizes, provides further evidence that the pore size distributions and subsequent capillary displacement and associated miscible transport models are reasonable representations of the experimental system. It is important to point out that once the pore structure was fixed, no other adjustable parameters were used to fit the dissolution model to the experimental data.

A notable feature of the pore-scale model presented herein is that the physical length of the model corresponds to the length of the sample used in the physical experiments (both of the order of 3 cm). Therefore we can compare directly the model results and the experimental results, and we can use the model to study upscaling behavior over the range from the pore scale to the physical core scale. In this study, we investigated the behavior of two macroscale mass transfer coefficients, K_{eff} and K_l . The rate coefficient K_{eff} corresponds to the coefficient that is derived from column studies of dissolution. This coefficient shows pronounced scaling effects in the problem studied, because of the development of a well-defined dissolution front whose width is much less than the overall column length. Averages over thin (1 mm) slices, oriented in the direction of the front, provided well-defined averages that differed significantly from those defined over the entire sample volume. This implies that care must be exercised in defining an effective mass transfer coefficient, especially when local fronts are involved. Note that the definition of K_{eff} incorporates local concentration gradients, so this behavior in the presence of a local concentration front is not completely unexpected. The more heuristic macroscopic mass transfer coefficient, K_l , shows much less scaling effects. In part, this is due to the fact

that its definition is independent of local concentration gradients and involves only volume averages of specific interfacial areas and local mass transfer coefficients. The dependence of K_{eff} on local concentration gradients serves to restrict the contributing interfacial areas to those in the zone of the active dissolution front. While the values of K_l were in the same range as K_{eff} for a certain NAPL content, the K_l values consistently overpredicted the actual mass transfer values.

Generally, we believe that these kinds of detailed pore-network models, in which the governing processes are defined at the appropriate length scales and subsequent upscaling can be performed in a consistent and well-defined way, provide a wealth of opportunities for investigation of different aspects of multiphase flow in porous media. These opportunities include investigations of underlying processes such as capillary displacement and dissolution, as well as investigations involving new variables such as interfacial area and new theories that seek to describe the behavior of these new variables. Until new experimental methods are developed to measure these nontraditional variables or to measure processes at highly resolved scales, pore-scale network models will provide unique opportunities to advance our knowledge of multiphase flow systems.

Acknowledgments. This work was supported in part by the National Science Foundation under grants EAR-9218803 and EAR-9805376 and by the Department of Energy under grant DE-FG07-96ER14703. Paul Reeves provided the capillary displacement code. We thank Helge Dahle, Lin Ferrand, Ulrich Fischer, Dan Goode, William Gray, Paul Imhoff, S. Majid Hassanizadeh, Carlo Montemagno, and Paul Reeves for helpful discussions and comments regarding this work.

References

- Delay, F., G. de Marsily, and E. Carlier, One-dimensional solution of the transport equation in porous media in transient state by a new numerical method for the management of particle track, *Comput. Geosci.*, 20(7/8), 1169–1200, 1994.
- Dillard, L. A., and M. J. Blunt, Development of a pore network simulation model to study nonaqueous phase liquid dissolution, *Water Resour. Res.*, 36(2), 439–454, 2000.
- Feenstra, S., and N. Guiguer, Dissolution of dense non-aqueous phase liquids in the subsurface, in *Dense Chlorinated Solvents and Other DNAPLs in Ground Water: History, Behavior and Remediation*, edited by J. Pankow and J. Jerry, chap. 7, pp. 203–232, Waterloo Educ. Serv., Waterloo, Ont., Canada, 1995.
- Geller, J. T., and J. R. Hunt, Mass transfer from nonaqueous phase organic liquids in water-saturated porous media, *Water Resour. Res.*, 29(4), 833–845, 1993.
- Gvirtsman, H., and P. V. Roberts, Pore-scale spatial analysis of two immiscible fluids in porous media, *Water Resour. Res.*, 27(6), 1165–1176, 1991.
- Hassanizadeh, S. M., and W. G. Gray, Thermodynamic basis of capillary pressure in porous media, *Water Resour. Res.*, 29(10), 3389–3405, 1993.
- Held, R. J., and M. A. Celia, Pore-scale modeling extension of constitutive relationships in the range of residual saturations, *Water Resour. Res.*, 37(1), 165–170, 2001.
- Imhoff, P. T., Dissolution of a nonaqueous phase liquid in saturated porous media, Ph.D. dissertation, Princeton Univ., Princeton, N. J., 1992.
- Imhoff, P. T., P. R. Jaffé, and G. F. Pinder, An experimental study of complete dissolution of a nonaqueous phase liquid in saturated porous media, *Water Resour. Res.*, 30(2), 307–320, 1994.
- Imhoff, P. T., M. H. Arthur, and C. T. Miller, Complete dissolution of trichloroethylene in saturated porous media, *Environ. Sci. Technol.*, 32(16), 2417–2424, 1998.
- Jia, C., K. Shing, and Y. C. Yortsos, Visualization and simulation of NAPL solubilization in pore networks, *J. Contam. Hydrol.*, 35, 363–387, 1999a.

- Jia, C., K. Shing, and Y. C. Yortsos, Advective mass transfer from stationary sources in porous media, *Water Resour. Res.*, 35(11), 3239–3251, 1999b.
- Johnson, J. A., V. Ravi, and J. K. Rumery, Estimation of solute concentration using the pathline method, *Ground Water*, 32(5), 719–726, 1994.
- Kennedy, C. A., and W. C. Lennox, A pore-scale investigation of mass transport from dissolving DNAPL droplets, *J. Contam. Hydrol.*, 24, 221–246, 1997.
- Lenormand, R., C. Zarcone, and A. Sarr, Mechanisms of the displacement of one fluid by another in a network of capillary ducts, *J. Fluid Mech.*, 135, 337–353, 1983.
- Li, Y., and N. C. Wardlaw, The influence of wettability and critical pore-throat size ratio on snap-off, *J. Colloid Interface Sci.*, 109, 461–472, 1986a.
- Li, Y., and N. C. Wardlaw, Mechanisms of nonwetting phase trapping during imbibition at slow rates, *J. Colloid Interface Sci.*, 109, 473–486, 1986b.
- Mayer, A. S., and C. T. Miller, The influence of porous medium characteristics and measurement scale on pore-scale distributions of residual nonaqueous-phase liquids, *J. Contam. Hydrol.*, 11, 189–213, 1992.
- Miller, C. T., M. M. Poirier-McNeill, and A. S. Mayer, Dissolution of trapped nonaqueous phase liquids: Mass transfer characteristics, *Water Resour. Res.*, 26(11), 2783–2796, 1990.
- Miller, C. T., G. Christakos, P. T. Imhoff, J. F. McBride, J. A. Pedit, and J. A. Trangenstein, Multiphase flow and transport modeling in heterogeneous media: Challenges and approaches, *Adv. Water Res.*, 21(2), 77–120, 1998.
- Mohanty, K. K., Fluid in porous media: Two-phase distribution and flow, Ph.D. dissertation, Univ. of Minn., Minneapolis, 1981.
- Mohanty, K. K., H. T. Davis, and L. E. Scriven, Physics of oil entrapment in water-wet rocks, *SPE Reservoir Eng.*, 2(1), 113–127, 1987.
- Powers, S. E., C. O. Loureiro, L. A. Abriola, and W. J. Weber Jr., Theoretical study of the significance of nonequilibrium dissolution of nonaqueous phase liquids in subsurface systems, *Water Resour. Res.*, 27(4), 463–477, 1991.
- Powers, S. E., L. A. Abriola, and W. J. Weber Jr., An experimental investigation of nonaqueous phase liquid dissolution in saturated subsurface systems: Steady state mass transfer rates, *Water Resour. Res.*, 28(10), 2691–2705, 1992.
- Powers, S. E., L. A. Abriola, and W. J. Weber Jr., An experimental investigation of nonaqueous phase liquid dissolution in saturated subsurface systems: Transient mass transfer rates, *Water Resour. Res.*, 30(2), 321–332, 1994.
- Reeves, P. C., The development of pore-scale network models for the simulation of capillary pressure-saturation-interfacial area-relative permeability relationships in multi-fluid porous media, Ph.D. dissertation, Princeton Univ., Princeton, N. J., 1997.
- Reeves, P. C., and M. A. Celia, A functional relationship between capillary pressure, saturation and interfacial area as revealed by a pore-scale model, *Water Resour. Res.*, 32(8), 2345–2358, 1996.
- Soerens, T. S., D. A. Sabatini, and J. H. Harwell, Effects of bypassing and nonuniform NAPL distribution on the mass transfer characteristics of NAPL dissolution, *Water Resour. Res.*, 34(7), 1657–1673, 1998.
- Young, D. F., and W. P. Ball, Effects of column conditions on the first-order rate modeling of nonequilibrium solute breakthrough, *Water Resour. Res.*, 31(9), 2181–2192, 1995.
- Zhou, D., L. A. Dillard, and M. J. Blunt, A physically based model of dissolution of nonaqueous phase liquids in the saturated zone, *Transp. Porous Media*, 39, 227–255, 2000.

M. A. Celia and R. J. Held, Environmental Engineering and Water Resources Program, Department of Civil and Environmental Engineering, Princeton University, Princeton, NJ 08544. (celia@princeton.edu; held@karst.princeton.edu)

(Received September 17, 1999; revised July 7, 2000; accepted September 1, 2000.)

